

Self-generated magnetic field in three-dimensional ablative Rayleigh-Taylor instability

Dehua Zhang¹, Xian Jiang¹, Tao Tao², Jun Li³, Rui Yan^{1,4,†}, De-Jun Sun¹, and Jian Zheng^{2,4}

¹Department of Modern Mechanics, University of Science and Technology of China, Hefei 230026, China

²Department of Plasma Physics and Fusion Engineering, University of Science and Technology of China, Hefei, Anhui 230026, China

³Institute of Applied Physics and Computational Mathematics, Beijing 100094, China

⁴IFSA Collaborative Innovation Center, Shanghai Jiao Tong University, Shanghai 200240, China

The self-generated magnetic field in three-dimensional (3D) single-mode ablative Rayleigh-Taylor instabilities (ARTI) relevant to the acceleration phase of a direct-drive inertial confinement fusion (ICF) implosion is investigated. It is found that stronger magnetic fields up to a few thousands of T can be generated by 3D ARTI than by its two-dimensional (2D) counterpart. The Nernst effects significantly alter the magnetic fields convection and amplify the magnetic fields. The scaling law for the magnetic flux obtained in the 2D simulations performs reasonably well in the 3D cases. While the magnetic field significantly accelerates the bubble growth in the short-wavelength 2D modes through modifying the heat fluxes, the magnetic field mostly accelerates the spike growth but has little influence on the bubble growth in 3D ARTI.

1. Introduction

The Rayleigh-Taylor instability (RTI) (Rayleigh 1900; Taylor 1950) is a fundamental hydrodynamic instability that occurs at the interface between heavy and light fluids when the heavy fluid is supported by the light fluid against gravity. RTI plays important roles in a number of astrophysical processes such as supernova explosions (Burrows 2000; Gamezo *et al.* 2003), and is considered as a critical risk in inertial confinement fusion (ICF) (Lindl 1998; Atzeni & Meyertervehn 2004) implosions. In a typical ICF experiment, a cold spherical deuterium and tritium (DT) target is irradiated either by direct laser light in the direct-drive (Craxton *et al.* 2015) approach, or by X-rays emitted by a high-Z hohlraum (Lindl 1998) in the indirect-drive (Lindl 1995; Lindl *et al.* 2004) approach. The energy absorbed near the target outer surface rapidly heats the material up and causes intense mass ablation off the target shell, leading to the shell's inward acceleration and compression. As the higher-density target shell is accelerated by the lower-density ablated plasma, the interface perturbed by initial surface roughness or irradiation non-uniformity is unstable to RTI which develops into an interchange of heavy with light fluids. The light fluid rises up forming “bubbles” while the heavy fluid falls down forming “spikes”. RTI dramatically degrades the implosion performances by compromising the shell integrity and mixing the inside deuterium-tritium (DT) fuel with the outside high-Z ablator. As the milestone on ignition has been recently achieved (Zylstra *et al.* 2022; Abu-Shawareb 2022) on the National Ignition Facility (NIF), further improved implosion performance and higher gain are being pursued in the future ICF designs where controlling the hydrodynamic instabilities remains a key factor to be considered.

As a candidate to improve ICF implosion performance, the applications of magnetic fields in

† Email address for correspondence: ruiyan@ustc.edu.cn

ICF have been attracting intensive research interests. An externally applied magnetic field has been proposed as a promising approach to improve ICF implosion performance by reducing the electron thermal conduction and magnetically confining the DT- α burning plasma in the hot spot (Wurden *et al.* 2016; Perkins *et al.* 2017). Enhanced fusion yield and temperature have been reported in cylindrical magnetized liner inertial fusion implosions (Slutz & Vesey 2012; Gomez *et al.* 2014) and magnetized direct-drive ICF implosions (Chang *et al.* 2011). Recent experiments at NIF have also demonstrated performance enhancement from an applied magnetic field in room-temperature (“warm”) indirect-drive implosions (Moody *et al.* 2022; Sio *et al.* 2023). The effects of externally applied magnetic fields on RTI in ICF-relevant conditions were also studied via numerical simulations (Walsh *et al.* 2017; Walsh 2022) and experiments (Matsuo *et al.* 2021). Walsh (2022) investigated the effects of externally applied external magnetic fields in different directions on the growth of the magnetized ARTI, considering both the magnetic tension and the magnetized heat flow, via three-dimensional (3D) extended-magnetohydrodynamics simulations. The experimental work by Matsuo *et al.* (2021) found that the external magnetic field reduces the electron thermal conduction across the magnetic field lines and enhances the ARTI growth.

Another type of magnetic field is self-generated by the plasmas and companies with the evolution of hydrodynamic instabilities. It was first predicted by the theoretical works that magnetic field can be generated in RTI in laser-produced plasmas (Stamper *et al.* 1971; Mima *et al.* 1978; Haines 1985; Stamper 1991). The Biermann-battery effect was identified as the key source generating magnetic field in RTI (Mima *et al.* 1978) : The misaligned temperature and density gradients generate magnetic fields via the nonzero $\nabla T_e \times \nabla n_e$, where T_e and n_e are the electron temperature and electron number density, respectively. In experiments, simultaneous Faraday rotation was utilized to diagnose the spontaneous magnetic field in laser-produced plasmas (Stamper & Ripin 1975; Raven *et al.* 1978; Stamper *et al.* 1978), but such diagnostic techniques used external optical probing and thus were inadequate to measure inside the high-density plasmas opaque to the probing lights (Wagner *et al.* 2004). Proton radiography was widely used to diagnose the laser-driven magnetic field structures under more extreme plasma parameters (Li *et al.* 2007, 2009; Gao *et al.* 2012, 2013, 2015; Manuel *et al.* 2012, 2015). The proton radiography experiments have shown that Mega-Gauss(MG)-level magnetic fields can be generated in RTI in laser-produced plasmas (Manuel *et al.* 2012, 2015; Gao *et al.* 2013).

Self-generated magnetic fields not only facilitate diagnostics on the deliberate fluid structures of RTI inside hot plasmas for the applications in proton radiography but may also influence hydrodynamic evolution if intense enough. While MG-level magnetic is not strong enough to directly affect the implosion hydrodynamics because the plasma thermal energy far exceeds the magnetic pressure (ie. the parameter $\beta \equiv 8\pi p/B^2 \gg 1$, where p is the pressure) in ICF-relevant plasmas, it may be strong enough to magnetize the plasma and alter the electron thermal conduction when the cyclotron frequency of the electron reaches the same order of magnitude as the electron collision frequency. The importance of the magnetic modification on electron thermal conductivity is often evaluated by the Hall parameter (Braginskii 1965) $\chi = \omega_{ce} \tau_e$, where ω_e is the electron cyclotron frequency, τ_e is the characteristic time of electron collisions. The self-generated magnetic fields due to RTI in ICF is largely determined by the mass ablation feature which brings rich physics to not only the hydrodynamics but also the generation and transportation of the magnetic fields.

When the intense laser energy is deposited on an ICF target shell, an ablated plasma outflow rapidly develops from the surface of shell (ablation front) and creates a high-temperature and low-density fluid relative to the unablated materials. The laser-driven RTI is characterized by this ablation process on the outer surface of the shell during the acceleration phase of the implosion, and the ablative RTI (ARTI) consequently behaves quite differently from the classical RTI (CRTI) due to the mass ablation near the ablation front. Mass ablation can stabilize RTI in the linear phase and results in a linear cutoff wave number k_c in the unstable spectrum (Takabe *et al.* 1985;

Betti *et al.* 1998) such that all modes with the perturbation wave number $k > k_c$ are linearly stable (Sanz 1994; Betti *et al.* 1995; Goncharov *et al.* 1996b), which is in contrast to CRTI where the growth rate is a monotonically increasing function of k . Unlike the stabilization effect during the linear phase, the vortexes inside the bubble generated by mass ablation destabilize RTI in the nonlinear phase in both two-dimensional (2D) and 3D ARTI by the vortex acceleration mechanism (Betti & Sanz 2006; Yan *et al.* 2016). The vorticity provides a centrifugal force to the bubble vertex and accelerates the nonlinear terminal bubble velocity (U_b^{rot}) above the classical value (U_b^{cl}), especially for the small-scale 3D bubbles (Betti & Sanz 2006; Yan *et al.* 2016). An asymptotic analysis of ICF-relevant ARTI was performed and the nonlinear evolution of the front was analyzed in 2D geometry by a boundary integral method in the case of a strong temperature dependence of the thermal conductivity (Almarcha *et al.* 2007).

The large temperature gradient created by the ablation provides the well-known Nernst effect (Nishiguchi *et al.* 1984) on the magnetic fields. The Nernst effect is known to provide an additional convective velocity against the direction of temperature gradient on the magnetic field, which will significantly affect the transport process of the magnetic field. One-dimensional (1D) simulations showed that the Nernst effect convects the magnetic field towards the high density region in laser-driven ablation plasma, and the magnetic field is significantly compressed and amplified (Nishiguchi *et al.* 1984, 1985).

The pioneering simulations (Srinivasan & Tang 2012; Srinivasan *et al.* 2012; Srinivasan & Tang 2013) were performed on the magnetic field generation and evolution for 2D single-mode and multimode RTI in a stratified two-fluid plasma using a Hall MHD model. However, neither the mass ablation due to heat conduction nor the Nernst effect was considered in those simulations. Our previous simulations (Zhang *et al.* 2022) including the heat conduction and the Nernst effect showed that ~ 100 T magnetic fields can be generated via ARTI and the Nernst effect is a critical factor determining the magnetic fields' peak amplitude and spacial distribution. As feedback to hydrodynamics, the self-generated magnetic field changes electron thermal conduction by magnetizing the plasma. The analytical study of the effects of self-generated magnetic fields on ARTI in the linear regime (García-Rubio *et al.* 2021) showed that the magnetic field affects the ARTI growth by bending the heat flux lines and it destabilizes ARTI for moderate Froude numbers (Fr) and stabilizes ARTI for large Fr , which is consistent with our 2D simulations (Zhang *et al.* 2022). The 2D simulations also showed that both the linear growth rate and the nonlinear amplitude of ARTI are increased by about 10% due to the magnetic feedback (Cui *et al.* 2024). The simulations on the stagnation phase of an ICF implosion showed that the magnetic field can cool the spikes and weaken the ablative stabilization, which harmfully increases the heat loss of hot spot (Walsh *et al.* 2017).

In this work, we present the simulation results for the evolution of the magnetic field generated via 3D ICF-relevant single-mode ARTI in a quasi-equilibrium frame of the acceleration phase of implosion. Important physics including ablation, Nernst, and magnetized heat conduction are taken into account to sketch more realistic magnetic fields' generation, evolution, and feedback to the ARTI evolution. It is found that $\sim 10^3$ T magnetic fields can be generated via 3D ARTI, which is an order of magnitude stronger than that found in our previous 2D work (Zhang *et al.* 2022). Such strong magnetic fields are able to profoundly alter local hydrodynamics by modifying the electron thermal conduction and speed up the growth of the spikes. The rest of the paper is organized as follows: section 2 outlines the physical model and the simulation settings. In section 3.1, the simulation results on the magnetic fields' generation and transportation are presented and analyzed. In section 3.2, the feedback of self-generated magnetic field on 3D ARTI nonlinear evolution is investigated. Section 4 is a summary.

2. Physics model and numerical method

The simulations on 3D ARTI and self-generated magnetic fields are carried out in planar geometry using the hydrodynamic code *ART*. Specifically designed for modeling ARTI in ICF-relevant scenarios, *ART* has been used in a number of recent works (Betti & Sanz 2006; Yan *et al.* 2016; Zhang *et al.* 2018, 2020; Xin *et al.* 2019, 2023; Zhang *et al.* 2022; Liu *et al.* 2023; Li *et al.* 2022, 2023, 2024; Fu *et al.* 2023). *ART* solves the single-fluid equations in 2D/3D Cartesian coordinates with the Spitzer-Harm thermal conduction (Spitzer & Härn 1953). The hydrodynamic equations are as follows:

$$\frac{\partial \rho}{\partial t} + \nabla \cdot (\rho \mathbf{v}) = 0, \quad (2.1)$$

$$\frac{\partial \rho \mathbf{v}}{\partial t} + \nabla \cdot (\rho \mathbf{v} \mathbf{v}) = -\nabla p + \rho \mathbf{g}, \quad (2.2)$$

$$\frac{\partial \varepsilon}{\partial t} + \nabla \cdot [(\varepsilon + p) \mathbf{v}] = \rho \mathbf{v} \cdot \mathbf{g}, \quad (2.3)$$

$$\rho c_v \frac{\partial T}{\partial t} = \nabla \cdot (\kappa_{sh} \nabla T), \quad (2.4)$$

where ρ is the mass density, \mathbf{v} is the macroscopic single-fluid velocity of the plasma, p is the plasma thermal pressure, and \mathbf{g} is the acceleration. Since $\beta \gg 1$, the magnetic forces are neglected in the momentum equation. The equation of state of an ideal gas is used, and the total energy is $\varepsilon = [p/(\gamma - 1)] + [\rho v^2/2]$ here. T is the kinetic temperature including the Boltzmann constant, $\gamma = 5/3$ is the specific heat ratio, and c_v is the constant-volume specific heat capacity. The single-temperature approximation of the plasma is applied so that the electron temperature T_e and ion temperature T_i are equal (ie. $T_e = T_i = T$). The thermal conduction part (2.4) is solved separately from the energy equation (2.3) in a Strang-splitting way (Strang 1968) and implicitly solved to avoid the strict time step Δt requirement of explicit diffusion equation solvers. The thermal conductivity coefficient κ_{sh} is given by the Spitzer-Harm model (Spitzer & Härn 1953) without flux-limiter as $\kappa_{sh} \propto T^{5/2}$. A MUSCL-Hancock scheme (van Leer 1984) with a HLLC (Harten *et al.* 1983) approximate Riemann solver is used as the hydrodynamic solver to achieve 2nd-order accuracy in both space and time. The single fluid is a DT plasma with the number ratio 1:1. The advantage of using a DT plasma in the simulations is that it can avoid complex physics such as radiation transport. Presently, neither radiation transport nor nonlocal electron heat conduction is included in our simulations of this paper.

The equation of magnetic field (\mathbf{B}) evolution can be readily derived from the Ampere's law, the Faraday's law, and the momentum equation of electrons (Nishiguchi *et al.* 1984) and formulated in Gaussian units as

$$\frac{\partial \mathbf{B}}{\partial t} = \underbrace{\nabla \times (\mathbf{v} \times \mathbf{B})}_I + \underbrace{\frac{c}{e} \nabla \times \left(\frac{\nabla p_e}{n_e} \right)}_{II} - \underbrace{\frac{c}{4\pi e} \nabla \times \left[\frac{(\nabla \times \mathbf{B}) \times \mathbf{B}}{n_e} \right]}_{III} - \underbrace{\frac{c}{e} \nabla \times \frac{\mathbf{R}}{n_e}}_{IV}, \quad (2.5)$$

where e is the elementary charge carried by an electron, c is the speed of light in vacuum, n_e and p_e are the number density and pressure of the electrons, respectively. $\mathbf{R} = \mathbf{R}_u + \mathbf{R}_T$ as the transfer of momentum from ions to electrons caused by collisions consists of two parts: (i) the thermal force \mathbf{R}_T due to the gradient of the electron temperatures and (ii) the friction force \mathbf{R}_u due to the relative velocity of electrons and ions. \mathbf{R}_T and \mathbf{R}_u are given as follows (Braginskii 1965):

$$\mathbf{R}_T = -\beta_{\parallel}^{uT} \nabla_{\parallel} T_e - \beta_{\perp}^{uT} \nabla_{\perp} T_e - \beta_{\wedge}^{uT} \mathbf{b} \times \nabla T_e \quad (2.6)$$

$$\mathbf{R}_u = -\alpha_{\parallel} \mathbf{u}_{\parallel} - \alpha_{\perp} \mathbf{u}_{\perp} + \alpha_{\wedge} \mathbf{b} \times \mathbf{u}, \quad (2.7)$$

where $\mathbf{b} \equiv \mathbf{B}/|\mathbf{B}|$ is the unit direction vector parallel to the magnetic field, $\mathbf{u} = \mathbf{u}_e - \mathbf{u}_i$ is

the relative velocity of electrons and ions which can be associated with the magnetic field via the Ampere's law: $\mathbf{u} = -c\nabla \times \mathbf{B}/(4\pi n_e e)$. $\nabla_{\parallel} T_e$ and $\nabla_{\perp} T_e$ are the components of the temperature gradient parallel and perpendicular to the direction of \mathbf{B} , respectively. \mathbf{u}_{\parallel} and \mathbf{u}_{\perp} are the components of \mathbf{u} parallel and perpendicular to the direction of \mathbf{B} , respectively. Here, β_{\parallel}^{uT} , β_{\perp}^{uT} , β_{\wedge}^{uT} , α_{\parallel} , α_{\perp} , and α_{\wedge} are the plasma transport coefficients, which are formulated as

$$\begin{aligned}\alpha_{\parallel} &= \frac{m_e n_e}{\tau_e} \alpha_0, & \alpha_{\perp} &= \frac{m_e n_e}{\tau_e} \left(1 - \frac{\alpha'_1 \chi^2 + \alpha'_0}{\Delta} \right), \\ \alpha_{\wedge} &= \frac{m_e n_e}{\tau_e} \frac{\chi(\alpha''_1 \chi^2 + \alpha''_0)}{\Delta} \\ \beta_{\parallel}^{uT} &= n_e \beta_0, & \beta_{\perp}^{uT} &= n_e \frac{\beta'_1 \chi^2 + \beta'_0}{\Delta}, \\ \beta_{\wedge}^{uT} &= n_e \frac{\chi(\beta''_1 \chi^2 + \beta''_0)}{\Delta},\end{aligned}$$

respectively, where m_e is electron mass, and the values of the coefficients α_0 , α'_0 , α''_0 , α'_1 , α''_1 , β_0 , β'_0 , β''_0 , β'_1 , β''_1 , and Δ can be found in Braginskii (1965). Improved transport coefficients were later obtained (Epperlein & Haines 1986; Ji & Held 2013; Davies *et al.* 2021) through fitting numerical solutions of the Fokker-Planck equation. It was reported in Davies *et al.* (2021) that the fitted transport coefficients can give physically incorrect results under certain conditions. We still utilize the classical Braginskii's coefficients in this work, also to be consistent with our previous work on 2D ARTI (Zhang *et al.* 2022) for a fair comparison.

Term I of (2.5) is usually known as the convection term that freezes the magnetic field along with the plasma. Term II is the baroclinic term (also known as the Biermann battery) generating the self-magnetic field through the misaligned density and pressure gradients, since $c\nabla \times (\nabla p_e / n_e) / e = c\nabla p_e \times \nabla n_e / (en_e^2)$. Term III is neglected since the ratio of III to II approximately equals to $1/\beta \ll 1$ in the regimes covered by this work. Term IV brings the effects of collisions, including the magnetic dissipation related to $\mathbf{R}_{\mathbf{u}}$ and the Nernst effect related to $\mathbf{R}_{\mathbf{T}}$. Bring in the expression of $\mathbf{R}_{\mathbf{T}}$ and $\mathbf{R}_{\mathbf{u}}$, term IV of (2.5) can be written as

$$\begin{aligned}\frac{\partial \mathbf{B}}{\partial t} &= \frac{c}{e} \nabla \times \left(\frac{\beta_{\parallel}^{uT} \nabla T_e}{n_e} \right) - \frac{c}{e} \nabla \times \left[\frac{(\beta_{\parallel}^{uT} - \beta_{\perp}^{uT})(\mathbf{b} \times \nabla T_e) \times \mathbf{B}}{B n_e} \right] - \frac{c}{e} \nabla \times \left(\frac{\beta_{\wedge}^{uT} \nabla T_e \times \mathbf{B}}{B n_e} \right) \\ &\quad - \frac{c^2}{4\pi e^2} \nabla \times \left\{ \frac{\alpha_{\parallel} \nabla \times \mathbf{B} - \alpha_{\wedge} \mathbf{b} \times (\nabla \times \mathbf{B}) - (\alpha_{\perp} - \alpha_{\parallel}) \mathbf{b} \times [\mathbf{b} \times (\nabla \times \mathbf{B})]}{n_e^2} \right\},\end{aligned}\quad (2.8)$$

The first term of the right hand of (2.8) has no contribution in a fully ionized plasma (Sadler *et al.* 2021) while the combination of the second and third terms can be rewritten as $\nabla \times [(\mathbf{V}_{\mathbf{N}} + \mathbf{V}_{\mathbf{CN}}) \times \mathbf{B}]$, where $\mathbf{V}_{\mathbf{N}}$ and $\mathbf{V}_{\mathbf{CN}}$ are often referred as the Nernst velocity and the cross-gradient Nernst velocity in the form of

$$\mathbf{V}_{\mathbf{N}} = -\frac{c\beta_{\wedge}^{uT}}{eBn_e} \nabla T_e, \quad (2.9)$$

$$\mathbf{V}_{\mathbf{CN}} = -\frac{c(\beta_{\parallel}^{uT} - \beta_{\perp}^{uT})(\mathbf{b} \times \nabla T_e)}{eBn_e}, \quad (2.10)$$

respectively. $\mathbf{V}_{\mathbf{N}}$ is along the opposite direction of ∇T_e so that it convects the magnetic field in the direction of the heat flow. $\mathbf{V}_{\mathbf{CN}}$ is in the direction of $-\mathbf{b} \times \nabla T_e$, which causes the magnetic field to convect along the isothermal line. $V_{\mathbf{N}}$ is much larger than $V_{\mathbf{CN}}$ where $\chi \sim T_e^{3/2} B / n_e \ll 1$, thus the contribution of $V_{\mathbf{N}}$ is dominating with moderate magnetic fields. The last term of the right hand of (2.8) reflects the diffusion of the magnetic field in different directions.

The intense magnetic field changes the process of electron heat conduction by magnetizing the plasma. While the magnetic field is not expected to be strong enough to significantly affect the implosion hydrodynamics via the momentum equation in ICF-relevant plasmas, it may be strong enough to magnetize the plasma and make the electron thermal conduction anisotropic via the Lorentz forces applied on the electrons moving in different directions with respect to the local

magnetic field. The heat flux in a magnetized plasma reads as

$$\mathbf{q}_{\text{mag}} = -\kappa_{\parallel} \nabla_{\parallel} T_e - \kappa_{\perp} \nabla_{\perp} T_e - \kappa_{\wedge} \mathbf{b} \times \nabla T_e, \quad (2.11)$$

where the detailed form of the magnetized plasma conduction coefficients κ_{\parallel} , κ_{\perp} and κ_{\wedge} can be found in Braginskii (1965). Along the direction parallel to \mathbf{B} , the magnetic field has no modification on the electron conduction and κ_{\parallel} is identical to κ_{sh} . κ_{\perp} is smaller than κ_{\parallel} where $B \neq 0$ and κ_{\perp} retreats to κ_{sh} where $B = 0$. κ_{\perp} decreases as χ increases, leading to a flux-limiting effect perpendicular to the magnetic fields. The term $-\kappa_{\wedge} \mathbf{b} \times \nabla T_e$ known as the Righi-Leduc heat flux makes a special contribution to the heat conduction in a magnetized plasma. Both (2.5) and (2.11) have been implemented in ART with the option to turn on and off different terms to be able to investigate a specific physical process.

In the ART simulations, ARTI is initialized to grow from small perturbations on top of a quasi-equilibrium state abstracted from a typical profile of direct-drive NIF targets as shown in figure 1. The initial hydro profiles of a DT ablator are similar to those of a 1.5 MJ direct-drive ignition target (McKenty *et al.* 2001) during the acceleration phase of an implosion. The cold and dense unablated DT shell is placed on top of the ablated DT plasma with a higher temperature but a lower density. The initial ablation front (the interface between the dense and the ablated plasma) is located at $z_0 = 70\mu\text{m}$ with the peak density $\rho_a = 5.3\text{g/cm}^3$ reached on the ablation front. The quasi-equilibrium state is obtained by integrating the 1D hydrodynamic equilibrium equations in the frame of reference of the shell from the ablation front toward both sides.

The ablation front is kept approximately fixed in space by balancing the ablative pressure with a dynamically adjusted effective gravity $g(t)$ which is initialized as $g(0) = 100\mu\text{m/ns}^2$. Since the shell mass decreases due to ablation, the effective acceleration $g(t)$ is slowly and automatically adjusted in time during the simulation to keep the ablation front approximately fixed in space, i.e., $g(t) = [(p + \rho u^2)_{bot} - (p + \rho u^2)_{top}] / M_{tot}$, where the subscripts ‘‘bot’’ and ‘‘top’’ indicate the integral values at the bottom and top boundaries, respectively, and M_{tot} is the total mass of the remaining plasma in the computational domain. This is equivalent to studying the ARTI growth in the frame of reference of the imploding shell. The quasi-equilibrium hydrodynamic profiles together with a time-dependent but spatially uniform gravity $g(t)$ are used to mimic an already well established quasi-equilibrium ICF plasma slowly evolving under the isobaric assumption also used in the analytical ARTI theories (Goncharov *et al.* 1996*b,a*). Our simulations do not include the underdense region where the lasers are interacting with the plasma, and therefore we do not directly handle laser absorption. Instead, the laser energy transported toward the ablation front is simulated by a constant bottom-boundary heat flow calculated self-consistently with the SH model on the basis of the 1D hydrodynamic profiles to ablate the target at an ablation velocity $V_a = 3.5\mu\text{m/ns}$ (i.e., the penetration velocity of the ablation front into the heavy shell material), and the corresponding ablation pressure (i.e., the pressure at the ablation surface) is $p_a = 130\text{Mbar}$.

In order to seed 3D ARTI, the velocity perturbations (\mathbf{v}_p) are initialized around the ablation front in a divergence-free form as

$$\begin{aligned} v_{px} &= v_{p0} \sin(kx) \exp(-k|z - z_0|), \\ v_{py} &= v_{p0} \sin(ky) \exp(-k|z - z_0|), \\ v_{pz} &= v_{p0} [\cos(kx) + \cos(ky)] \exp(-k|z - z_0|), \end{aligned}$$

where v_{p0} is the magnitude of the initial velocity perturbation set as $v_{p0} = 0.5\mu\text{m/ns}$, $k \equiv 2\pi/\lambda$ is the perturbation wavenumber, and λ is the perturbation wavelength. A typical simulation is carried out with a simulation box of $140\mu\text{m}$ in the z direction, while the widths in the x and y directions are chosen to be λ . A uniform Cartesian grid is used with the resolution of 10 grid points per $1\mu\text{m}$ and the grid independence is checked to ensure numerical convergence. Periodic

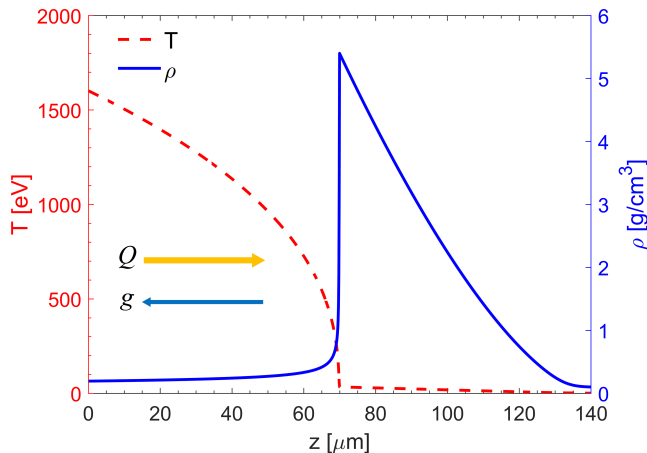


FIGURE 1. The initial profile for ρ (solid line) and T (dashed line) along the z axis.

boundary conditions are applied in the x and y directions and the inflow/outflow boundary conditions are used on the upper/lower boundaries along the z direction.

3. Results and discussions

A series of ART simulations have been performed to study the generation, evolution, and feedback of the self-generated magnetic fields accompanying ARTI in 3D geometry. As outlined in section 2, we have setup an idealized but still experimentally relevant scenario to be able to focus on the pure ARTI evolution and the magnetic generation in the ART simulations. This approach also enables us to conveniently investigate the factors (i.e., geometric dimensions, ablation, the Nernst effects, and magnetized heat fluxes) that influence RTI and/or magnetic evolution by switching these modules in the simulations on and off while still allowing the simulations to start from virtually the same quasi-equilibrium hydrodynamic state, for a relatively fair comparison. The detailed simulation parameters spanning a range of λ , V_a , p_a , and g_0 are listed in table 1. Our previous 2D work (Zhang *et al.* 2022) demonstrated that the effects involving the self-generated magnetic fields are more profound for short-wavelength modes with λ close to the linear cutoff wavelength $\lambda_c \equiv 2\pi/k_c$. Therefore, the simulation cases are more focused on the short wavelength regime in this work.

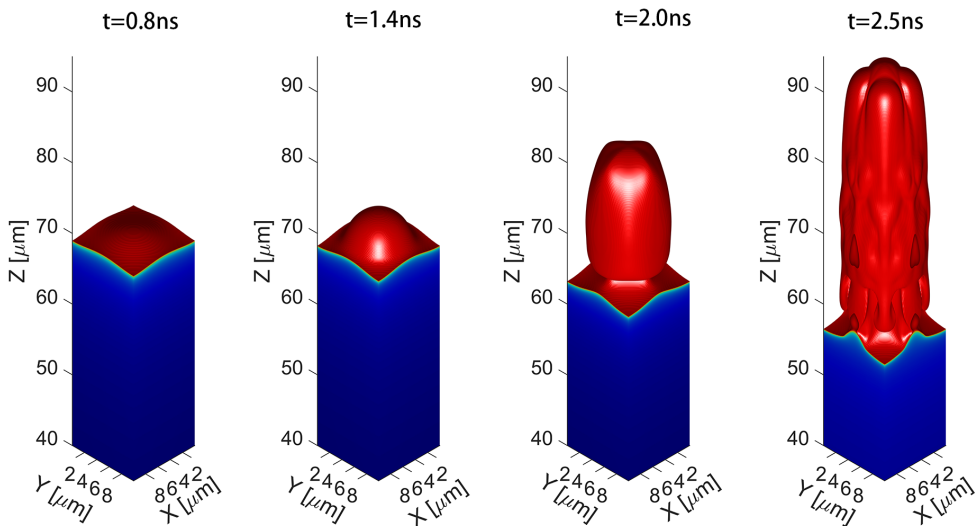
3.1. Evolution of the self-generated magnetic field

The evolution of ARTI from the linear stage up to the highly nonlinear stage in Case i is illustrated in figure 2. It is shown that a clear 3D bubble is formed in the center of the simulation box as the perturbation amplitude increases, with the high-density fluid surrounding the bubble penetrating down into the low-density fluid. The “bubble-spike” topology is significantly different from its 2D counterpart.

The magnetic field generation is found correlated with the growth of ARTI. The magnetic fields at the linear stage in Cases i (without Nernst) and ii (with Nernst) are illustrated in figure 3(a) and (b) respectively. Figure 3(a) shows that the magnetic fields are mostly generated near the ablation front where the baroclinic source i.e. term II of (2.5) is concentrated. The generated magnetic field then expands with the ablated material and enters the low-density area by convection. As a result, a magnetic field layer is formed below the ablation front. Case ii with the Nernst effects turned on clearly shows the influence from \mathbf{V}_N and \mathbf{V}_{CN} which are largely

Case	2D/3D	λ (μm)	V_a ($\mu\text{m}/\text{ns}$)	p_a (Mbar)	g_0 ($\mu\text{m}/\text{ns}^2$)	V_N	V_{CN}	q_{mag}
i	3D	10	3.5	140	100	off	off	off
ii	3D	10	3.5	140	100	on	on	off
iii	3D	10	3.5	140	100	on	off	off
iv	2D	10	3.5	140	100	on	on	off
v	3D	10	2.75	140	100	on	on	off
vi	3D	10	2.0	140	100	on	on	off
vii	3D	10	3.5	200	100	on	on	off
viii	3D	10	3.5	300	100	on	on	off
ix	3D	10	3.5	140	120	on	on	off
x	3D	10	3.5	140	80	on	on	off
xi	3D	6	3.5	140	100	on	on	off
xii	3D	20	3.5	140	100	on	on	off
xiii	3D	30	3.5	140	100	on	on	off
xiv	3D	6	3.5	140	100	on	on	on
xv	3D	10	3.5	140	100	on	on	on
xvi	3D	20	3.5	140	100	on	on	on
xvii	3D	30	3.5	140	100	on	on	on

TABLE 1. Parameters and physical options of the ART simulations

FIGURE 2. The ARTI bubble structure at different times, from the linear stage [$t = 0.8\text{ns}$] to the nonlinear stage [$t = 1.4, 2.0$ and 2.5ns], in Case i.

determined by the amplitude of the magnetic field and ∇T_e [see (2.9) and (2.10)]. The Nernst velocity V_N tends to convect the magnetic field against the ablation front [figure 3(b)], where T_e transits abruptly from the cold dense shell to the ablated low-density plasma thus V_N is towards the shell. The cross gradient Nernst velocity V_{CN} tends to transport the magnetic field towards the central axis of the bubble, illustrated by the arrows in figure 3(b). V_{CN} is read in the simulations to be much smaller than V_N at the linear stage, consistent with the small Hall parameter at this moment [$\chi_{\text{max}} \ll 1$ as plotted in figure 7(c)]. The Nernst effects lead to a stronger magnetic

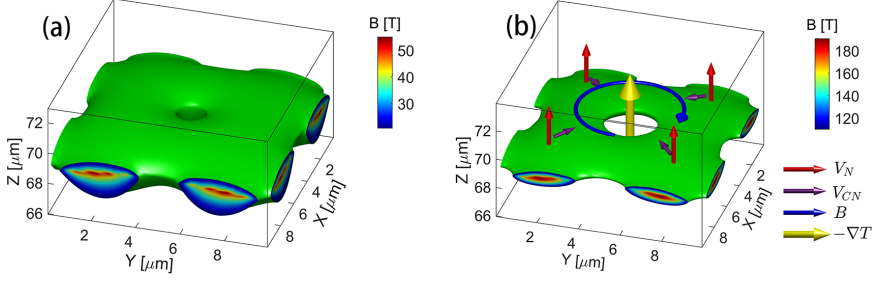


FIGURE 3. Magnetic field at the linear stage [$t = 0.8$ ns] of ARTI. (a) Magnetic field isosurface at $B = 20$ T in Case i. (b) Magnetic field isosurface of $B = 105$ T in Case ii, with the colored arrows illustrating the schematic of \mathbf{V}_N , \mathbf{V}_{CN} , \mathbf{B} , and $-\nabla T$ near the ablation front.

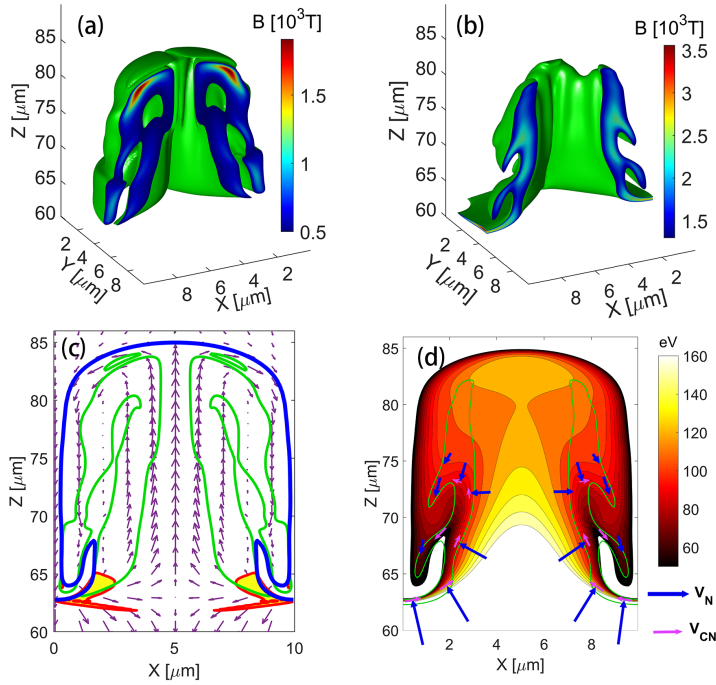


FIGURE 4. Comparison of self-generated magnetic fields at the highly nonlinear stage [$t = 2.0$ ns] of 3D ARTI with and without the Nernst effect. (a) Magnetic field isosurface at $B = 500$ T in Case i. (b) Magnetic field isosurface $B = 1400$ T in Case ii. (c) Schematic diagram illustrating the transport of magnetic field with the plasma inside the bubble, taken at a slice passing through the bubble axis in Case i. Arrows denote fluid velocities relative to the bubble, defined as velocities of the light fluid within the bubble minus the penetration velocity of the bubble vertex into the denser fluid. The blue line represents the bubble interface, while the green lines indicate the magnetic field contours at 500T. Yellow areas enclosed by red lines denote the regions where the baroclinic term exceeds 5000T/ns. (d) Temperature contours inside the bubble at the slice passing through the bubble axis in Case ii. The green lines are the magnetic field contours at 1400T. The arrows of different colors depict the schematic diagrams of \mathbf{V}_N and \mathbf{V}_{CN} inside the bubble.

field in a thinner layer below the ablation front with the peak value of the magnetic field B_{peak} amplified by more than three times.

It is usually considered that ARTI enters the nonlinear stage when the perturbation amplitude grows larger than 0.1λ and a “bubble” emerges. In the nonlinear stage the growth of the

ARTI bubble is subject to the vortex dynamics near the ablation front and inside the bubble. The magnetic fields in Cases i (without Nernst) and ii (with Nernst) are shown in figure 4 for comparison. Figure 4(a) shows a complicated magnetic ring inside the bubble in Case i while a slice passing the bubble axis is plotted in figure 4(c) to illustrate the transportation of the magnetic field. As the large-amplitude bubble is formed, the fluid inside the bubble gets cooled down [see figure 4(d)] thus the ablation on the interface inside the bubble is almost inhibited. Intense ablation is mostly concentrated on the “spike” tips where the baroclinic source generating magnetic fields also reaches the maximum as shown by the yellow areas in figure 4(c). Then the magnetic field is transported into the bubble along with the fluid convection. The arrows demonstrate the fluid velocities relative to the bubble motion, namely how the ablated light fluid carrying the magnetic field moves around inside the bubble. The ablated light fluid first moves upward toward the bubble vertex then downward guided by the bubble wall, forming a fairly complicated magnetic ring. The magnetic field reaches the maximum at the top of the bubble in Case i, as shown in figure 4(a).

Due to the similarity of the equations on the magnetic field evolution (2.5) and on the vortex dynamics, the evolution of the magnetic field without Nernst effect is quite similar to the evolution of vorticity $\omega \equiv \nabla \times \mathbf{v}$. (2.5) retreats to $\partial_t \mathbf{B} = \nabla \times (\mathbf{v} \times \mathbf{B}) + (cm_i/2e)\nabla \times (\nabla p/\rho)$ for a DT plasma if not considering the resistivity or Nernst effect, where m_i is the average ion mass, while $\partial_t \omega = \nabla \times (\mathbf{v} \times \omega) - \nabla \times (\nabla p/\rho)$ describes the vorticity evolution in a non-viscous fluid with conservative body force. The self-generated magnetic field can be considered as an approximate signature of the vorticity in a non-Nernst fluid since $\mathbf{B} \approx -(cm_i/2e)\omega$, which is verified in the simulation of Case i.

The Nernst effects are found to alter the magnetic field distribution in the nonlinear stage of ARTI in Case ii, as shown in figure 4(b) and (d). Compared to its non-Nernst counterpart in Case i, the magnetic fields are more concentrated towards the spike tips and reach much higher magnitudes by roughly 2 times. The peak value of the magnetic field B_{peak} with the Nernst effect is approximately 3.5kT, whereas B_{peak} without the Nernst effect is around 1.8kT. Figure 4(d) shows the slice passing the bubble axis to illustrate the temperature distribution inside the bubble, which largely determines \mathbf{V}_N and \mathbf{V}_{CN} . The schematic on the directions of \mathbf{V}_N and \mathbf{V}_{CN} is also demonstrated with the arrows. The fluid inside the bubble gets rapidly cooled down once leaving the spike tips, forming an intense temperature gradient and a very large \mathbf{V}_N inside the bubble towards the spike tips. So the magnetic field is compressed by the \mathbf{V}_N convection to a smaller area close to the spike tips compared to the non-Nernst Case i [figure 4(a)]. The cross gradient Nernst velocity \mathbf{V}_{CN} tends to convect the magnetic field along the isotherm surfaces. However, as $V_{CN} \ll V_N$ is found in Case ii, the \mathbf{V}_{CN} convection is expected to be less important than the \mathbf{V}_N convection, which is further verified by comparing to Case iii where \mathbf{V}_{CN} is neglected. The magnetic distributions in Cases ii and iii are very similar.

Moreover, the growth of the magnetic fluxes ($\phi \equiv \int |B| dS$ on an area passing the bubble axis and inside the bubble), which was used to evaluate an average intensity of the magnetic field (Zhang *et al.* 2022), with the ARTI bubble amplitude h_b throughout a series of 3D and 2D simulations (Cases i-iv) with/without Nernst effects are plotted in figure 5. Cases i-iv use the same perturbation wavelength $\lambda = 10\mu\text{m}$. It was found that ϕ inside 2D ARTI bubbles are monotonically correlated with h_b in our previous research, and can be well formulated by a scaling law, no matter if the Nernst effects are included (Zhang *et al.* 2022). It was also found that the Nernst velocity affects the convection process but not the generation of magnetic field and has little impact on ϕ in the 2D cases. Figure 5 shows that ϕ in the 3D cases have similar behaviors to that in the 2D cases, as ϕ increases monotonically with h_b . While the peak value of the 3D magnetic field (about 3.5kT) is much larger than that of 2D (about 1.5kT), 3D ϕ (Cases ii and iii) is just slightly larger than 2D ϕ (Case iv) at the same h_b . Among the 3D cases, ϕ with the Nernst effects (Cases ii and iii) is just slightly larger than the non-Nernst ϕ (Case i), indicating

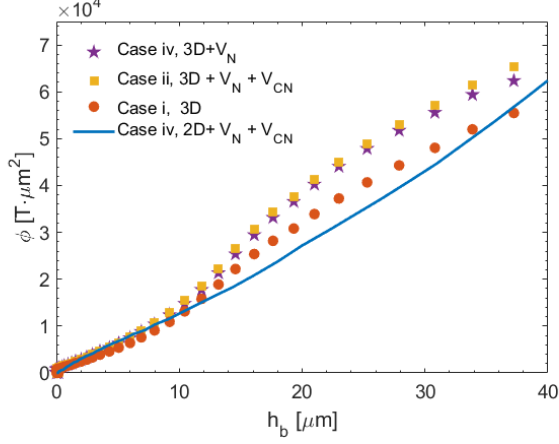


FIGURE 5. The magnetic fluxes ϕ inside the bubble at different ARTI amplitudes (h_b), where ϕ is defined as $\phi \equiv \int |B| dS$ at the slice of $y = \lambda/2$, and h_b is defined as the height from the bubble vertex to the spike tip.

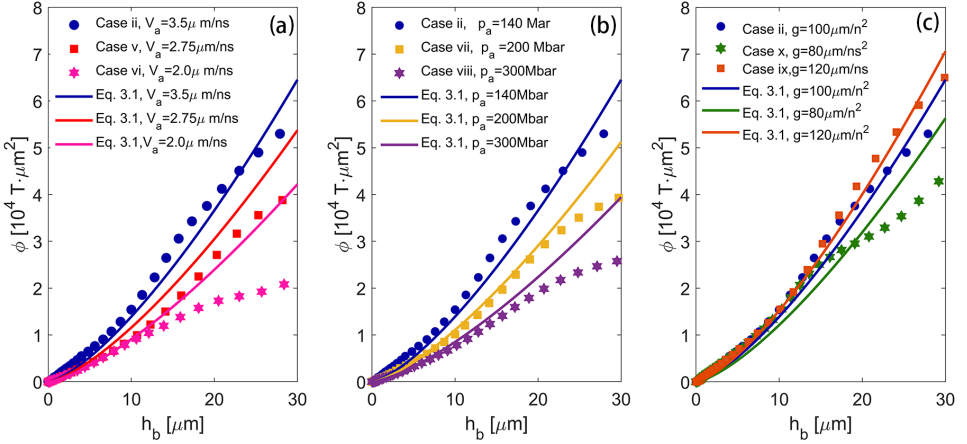


FIGURE 6. The magnetic fluxes ϕ of $10\mu\text{m}$ simulations (Case ii,v-x). (a) The circles: Case ii. The squares: Case v. The stars: Case vi. (b) The circles: Case ii. The squares: Case vii. The stars: Case viii. (c) The circles: Case ii. The squares: Case ix. The stars: Case x. The solid lines in (a), (b), and (c) represent ϕ obtained by applying the magnetic flux scaling law (3.1) to the parameters of the cases with the same color, where $V_0 \equiv \sqrt{p_a/\rho_a}$, $g_0 \equiv p_a/(\rho_a\lambda)$, $\phi_0 \equiv cm_i\lambda\sqrt{p_a/\rho_a}/e$, $b = 41.55$, $\xi = 1.397$, $\eta = 0.759$, and $\theta = 0.267$.

that the Nernst effects have mild impact on ϕ , which is qualitatively consistent with the findings in 2D reported in Zhang *et al.* (2022). The small difference on ϕ between Case ii and Case iii is also evidencing that the influence of V_{CN} is insignificant.

We then examine if the scaling law for ϕ obtained in the 2D cases (Zhang *et al.* 2022) is applicable in the 3D cases. The scaling law reads

$$\frac{\phi}{\phi_0} = b\left(\frac{h}{\lambda}\right)^\xi \left(\frac{V_a}{V_0}\right)^\eta \left(\frac{g}{g_0}\right)^\theta, \quad (3.1)$$

where $V_0 \equiv \sqrt{p_a/\rho_a}$, $g_0 \equiv p_a/(\rho_a\lambda)$, and $\phi_0 \equiv cm_i\lambda\sqrt{p_a/\rho_a}/e$. The coefficients $b = 41.55$, $\xi = 1.397$, $\eta = 0.759$ and $\theta = 0.267$ were fitted using the 2D simulation data. The scaling law (3.1) demonstrates positive correlations between ϕ and V_a and g , and a negative correlation

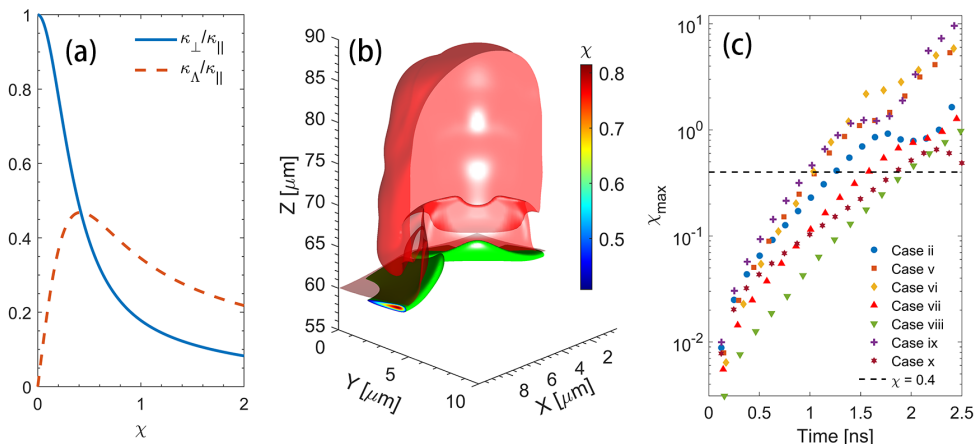


FIGURE 7. Hall parameter in ARTI. (a) The ratios of $\kappa_{\perp}/\kappa_{\parallel}$ and $\kappa_{\wedge}/\kappa_{\parallel}$ at different χ values. (b) Hall parameter at $t = 2.0\text{ns}$ in Case ii. The red surface is the bubble interface, and the green surface is the isosurface of the Hall parameter at $\chi = 0.4$. (c) The peak value of Hall parameter χ_{\max} vs. time in Cases ii and v-x, all with the Nernst effects included.

between ϕ and p_a . Figure 6(a), (b), and (c) plot the curves of ϕ versus h_b in Cases ii and v-x at different values of V_a , p_a , and g , respectively. It is shown that larger V_a or g lead to larger ϕ at the same h_b in figure 6(a) and (c), while figure 6(b) shows that smaller p_a leads to a faster ϕ growth with h_b . These trends are consistent with the prediction of the scaling law (3.1). Moreover, figure 6 shows that the 2D scaling law works reasonably well predicting ϕ in the 3D cases when h_b is small. Larger deviations between the simulations and the predictions of the scaling law (3.1) show up as h_b becomes larger, which is likely due to the 3D effects including the more complicated 3D magnetic structures inside the bubble.

As the magnitude of the magnetic field increases with h_b , the modification on the heat conduction is expected to be more significant. The heat flux perpendicular to the magnetic field $\mathbf{q}_{\perp} \equiv -\kappa_{\perp}\nabla_{\perp}T_e$ is mitigated while the Reghi-Leduc heat flux $\mathbf{q}_{\text{RL}} \equiv -\kappa_{\wedge}\mathbf{b} \times \nabla T_e$ that was absent in a magnetic-free plasma shows up to contribute to heat conduction. The significance of the magnetic modifications on the heat conduction is usually evaluated by the Hall parameter χ . Figure 7(a) shows the dependence of the ratios of κ_{\perp} and κ_{\wedge} to κ_{\parallel} on χ in a DT plasma. It is shown that $\kappa_{\perp}/\kappa_{\parallel}$ decreases monotonically with the increase of χ , while $\kappa_{\wedge}/\kappa_{\parallel}$ reaches the maximum at $\chi \approx 0.4$ where $\kappa_{\perp}/\kappa_{\parallel}$ drops by about a half. It is convenient to define a characteristic $\chi_c = 0.4$ such that the feedback of magnetic field to the heat conduction is considered to be significant where χ approaches or even exceeds χ_c .

Figure 7(b) illustrates the isosurface (green) where $\chi = \chi_c$ of Case ii in the highly nonlinear stage at $t = 2.0\text{ns}$. It shows that large χ is mainly concentrated near the spike tip, and the peak value of χ can be larger than 0.8. The maximum of χ in Cases ii and v-x with different physical parameters (V_a , g , and p_a) and all including the Nernst effects are plotted in figure 7(c). It is shown that χ_c can be reached in all cases, which indicates that the feedback of the self-generated magnetic field on the thermal conduction and consequently on the hydrodynamics could be significant with ICF-relevant parameters. It was found that the magnetic field boosts the ARTI bubble velocities of the short-wavelength modes while has minimal effects on the long-wavelength modes in 2D simulations (Zhang *et al.* 2022). The 3D simulations including the feedback are discussed in section 3.2 as follows.

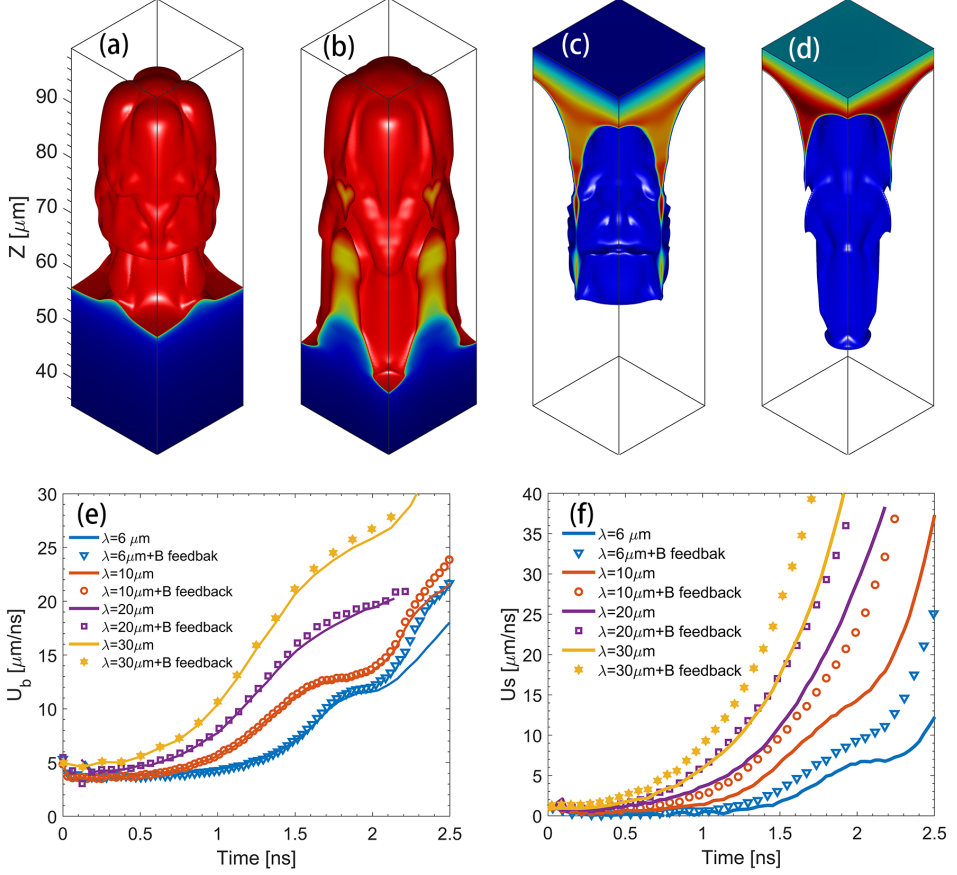


FIGURE 8. (a-d) ARTI bubble and spike structures in the highly nonlinear stage [$t = 2.5$ ns] for the case without [Case ii] and with [Case xv] magnetic feedback. (a) and (c) are bubble and spike of the case without magnetized heat flux [Case ii]. (c) and (d) are bubble and spike of case with magnetized heat flux [Case xv]. The spike structures are plotted from data after the bubble translation to better demonstrate the effect of magnetic field feedback on spike growth. The bubble velocity U_b (e) and the spike velocity U_s (f) in the different wavelength cases without [solid lines] and with [markers] magnetic feedback. The bubble velocity U_b and the spike velocity U_s are defined as the velocity of the vertex of the bubble and the spike relative to the velocity of the dense target plasma averaged in x-y plane.

3.2. Effects of magnetized heat flux on the growth of 3D ARTI

To investigate the feedback of the magnetic field on the hydrodynamic evolution in ARTI, a series of simulations [Cases xiv-xvii] using the magnetized heat flux described by (2.11) are performed. The non-feedback cases [ii, xi-xiii] with the same other parameters but using the classical non-magnetized Spitzer-Harm heat flux are available for comparison. Four wavelengths [6, 10, 20 and $30 \mu\text{m}$] are selected in order to investigate the magnetic feedback at different wavelengths. The Nernst effects are always turned on in these simulation cases in this section to take into account the Nernst enhancement on the magnetic field as well as χ .

The magnetized heat fluxes are found to significantly alter the ARTI bubble and spike structures in the nonlinear stage. Figs. 8(a)/(c) and (b)/(d) compare the $\lambda = 10 \mu\text{m}$ ARTI bubble/spike structures without [Case ii] and with [Case xv] the magnetized heat flux at the same time [$t = 2.5$ ns], respectively. It is shown that the magnetic feedback has little impact on the bubble evolution as the position of the bubble vertex with the magnetized heat flux [figure 8(b)] is only

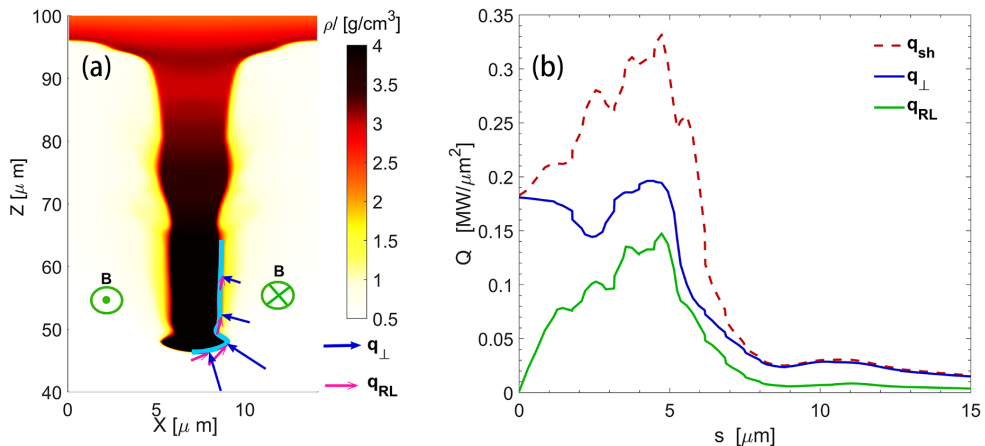


FIGURE 9. (a) Density contour in the slice of $y = x$ and the schematic diagram of the magnetic field direction surrounding the spike in the nonlinear stage [$t = 2.5\text{ns}$] for the $10\mu\text{m}$ wavelength case with magnetic feedback [Case xv]. The blue and pink arrows are the schematic diagram of \mathbf{q}_\perp and \mathbf{q}_{RL} , respectively. (b) Heat flux at the spike interface [cyan curve in (a)] vs s , s is defined as the distance on the cyan curve to the spike vertex.

slightly higher than the non-feedback case [figure 8(a)]. However, the magnetized heat flux has a significant impact on the growth and structure of the spikes, as shown in figure 8(c) and (d). The spike [figure 8(d)] with the magnetized heat flux is longer and finer than that [figure 8(c)] without the magnetized heat flux.

Moreover, the bubble velocity U_b and the spike velocity U_s without and with magnetic feedback are plotted in figure 8(e) and (f) for the simulations with different perturbation wavelengths to demonstrate the distinguished magnetic effects on the bubble and spike growths in 3D ARTI. It is shown that the magnetized heat flux has mild modifications on U_b in the cases with $\lambda \geq 10\mu\text{m}$, while just slightly increases U_b in the $\lambda = 6\mu\text{m}$ case in the highly nonlinear stage [$t > 2.0\text{ns}$]. However, U_s is increased more significantly than U_b due to the magnetized heat flux in all the cases with different λ , as shown in figure 8(f). The behaviors of U_b in the 3D cases are substantially different from the results in the 2D simulations (Zhang *et al.* 2022) where the magnetized heat flux significantly increases the short-wavelength ($\lambda \leq 15\mu\text{m}$) U_b in 2D. The magnetic modifications on U_b in both 2D and 3D can be attributed to the ablation weakening near the spike tip.

The schematic of the magnetic fields, the magnetic-perpendicular heat flux \mathbf{q}_\perp , and the Reghi-Leduc heat flux \mathbf{q}_{RL} near a 3D spike are illustrated on top of the density contour in the highly nonlinear stage of Case xv in figure 9 (a). As ∇T_e is perpendicular to the magnetic field on the plane shown in figure 9(a), the heat flux \mathbf{q}_\perp along $-\nabla T_e$ is reduced by the magnetic field, while the presence of \mathbf{q}_{RL} tends to guide the heat flux along the surface of the spike toward the inside of the bubble. Figure 9(b) further plots the heat flux components on the surface of the spike versus the distance s on the cyan curve to the spike vertex. The unmagnetized classical Spitzer-Harm heat flux q_{sh} is also plotted for comparison. It is shown that the strongest ablation is concentrated on the area near the spike tip as q_\perp is large near the spike tip ($s < 5\mu\text{m}$). q_\perp is equivalent to q_{sh} on the spike vertex ($s = 0$) where it is magnetic-free. Elsewhere q_\perp is significantly smaller than q_{sh} near the spike tip, leading to weaker ablation on the spike. The Regi-Leduc heat flux whose peak value is comparable to q_\perp tends to transport more heat into the bubble away from the spike vertex, which also helps to reduce the ablation near the spike tip. The weakened ablation helps to form the long spike in the magnetized-heat-flux Case xv as shown in figure 8(d). The different efficacy

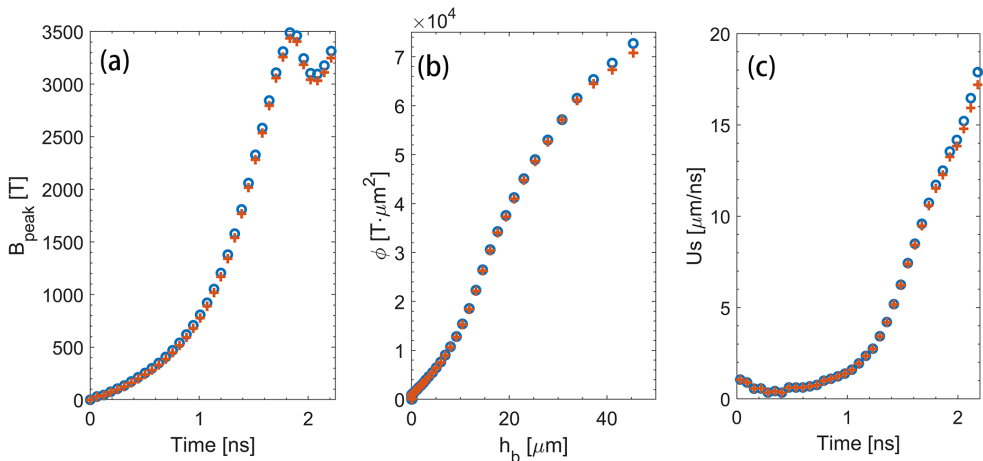


FIGURE 10. B_{peak} (a), ϕ (b) and U_s (c) without (circles) and with (crosses) the magnetic field energy sink in the energy equation (2.3).

of the magnetic feedback boosting the bubble velocity in 2D and 3D is likely due to the different compressibility of the bubble in 2D and 3D. The width of a 2D bubble has to be squeezed as the spike gets wider due to the reduction of ablation and smaller bubble width is known to lead to stronger vorticity inside which supplies a stronger lifting force to the bubble vertex through the vortex acceleration mechanism (Zhang *et al.* 2022; Betti & Sanz 2006). However, a 3D bubble is more difficult to squeeze as it always tends to expand itself to form a round bubble. As shown in figure 8(a) and (b), the sizes of the upper part of the 3D bubbles in the cases with and without magnetic feedback are not notably different, which indicates that the vortex acceleration on a 3D bubble is not significantly enhanced by the magnetic feedback.

In the cases presented so far (Cases i-xvii), the magnetic field energy have not been coupled in (2.3) in the large- β regime where the magnetic field energy is negligible compared to the plasma internal energy. However, the locally concentrated intense magnetic fields up to a few thousands of T generated in the highly nonlinear ARTI stages brings our attention on the validation of the modeling. We then take the magnetic field energy into account in the energy equation (2.3) by putting the Biermann battery source to the magnetic field as an energy sink from the plasma internal energy. The simulation with the magnetic field energy sink are also performed, which has the same other simulation configurations as Case ii. The results of the simulation with the magnetic field energy sink and Case ii are plotted in figure 10. It is shown that magnetic field energy sink has a very small influence on the B_{peak} , ϕ , and U_s in the highly nonlinear stage, indicating that the magnetic field energy sink is unimportant in this regime.

4. Summary

The self-generated magnetic field in 3D single-mode ARTI is numerically investigated with the parameters relevant to direct-drive ICF. This study finds that 3D ARTI can produce much stronger magnetic fields, reaching magnitudes up to a few thousand T, compared to its 2D counterpart. Similar to the 2D cases, the inclusion of the Nernst effect significantly alters magnetic field convection and amplifies magnetic fields from the linear to the nonlinear stage of ARTI. The magnetic field is compressed toward the spike tip by the Nernst effect, reaching approximately twice of the peak magnitude in the non-Nernst case. Moreover, it is found that the influence coming from \mathbf{V}_{CN} on the magnetic field convection is less significant than that from \mathbf{V}_N . The scaling law for the magnetic flux obtained from the 2D simulations performs reasonably well in

the 3D cases, showing qualitatively similar dependence of the magnetic flux on V_a , p_a , and g in 2D and 3D.

In many 3D cases the Hall parameter can reach a characteristic value of $\chi_c = 0.4$, beyond which the magnetized heat flux deviating significantly from the unmagnetized classical Spitzer-Harm heat flux is able to affect ARTI evolution. Unlike the magnetic field significantly accelerates the bubble growth in the short-wavelength 2D modes, the magnetic field mostly accelerates the spike growth but has little influence on the bubble growth in 3D ARTI. The spike acceleration due to magnetic feedback is attributed to the ablation reduction near the spike tip.

This research was supported by the National Natural Science Foundation of China (NSFC) under Grant Nos. 12175229 and 12388101, by the Strategic Priority Research Program of Chinese Academy of Sciences under Grant Nos. XDA25050400 and XDA25010200, by the Science Challenge Project, and by the Fundamental Research Funds for the Central Universities. The numerical calculations in this paper have been done on the supercomputing system in the Supercomputing Center of University of Science and Technology of China.

Declaration of Interests. The authors report no conflict of interest.

REFERENCES

- ABU-SHAWAREB, ET AL 2022 Lawson criterion for ignition exceeded in an inertial fusion experiment. *Phys. Rev. Lett.* **129**, 075001.
- ALMARCHA, C., CLAVIN, P., DUCHEMIN, L. & SANZ, J. 2007 Ablative rayleigh-taylor instability with strong temperature dependence of the thermal conductivity. *Journal of Fluid Mechanics* **579**, 481–492.
- ATZENI, S. & MEYERTERVEHN, J. 2004 The physics of inertial fusion: Beam plasma interaction, hydrodynamics, hot dense matter. *Physical Review Letters* **58** (7), 91–95.
- BETTI, R., GONCHAROV, V. N., MCCRORY, R. L. & VERDON, C. P. 1995 Self-consistent cutoff wave number of the ablative Rayleigh-Taylor instability. *Physics of Plasmas* **2** (10), 3844–3851.
- BETTI, R., GONCHAROV, V. N., MCCRORY, R. L. & VERDON, C. P. 1998 Growth rates of the ablative Rayleigh-Taylor instability in inertial confinement fusion. *Physics of Plasmas* **5** (5 PART 1), 1446–1454.
- BETTI, R. & SANZ, J. 2006 Bubble acceleration in the ablative Rayleigh-Taylor instability. *Physical Review Letters* **97** (20), 1–4.
- BRAGINSKII, S. I. 1965 Transport processes in a plasma. *Reviews of Plasma Physics* **1**, 205.
- BURROWS, ADAM 2000 Supernova explosions in the Universe. *Nature* **403** (6771), 727–733.
- CHANG, P. Y., FIKSEL, G., HOHENBERGER, M., KNAUER, J. P., BETTI, R., MARSHALL, F. J., MEYERHOFER, D. D., SÉGUIN, F. H. & PETRASSO, R. D. 2011 Fusion yield enhancement in magnetized laser-driven implosions. *Physical Review Letters* **107** (3), 2–5.
- CRAXTON, R. S., ANDERSON, K. S., BOEHLY, T. R., GONCHAROV, V. N., HARDING, D. R., KNAUER, J. P., MCCRORY, R. L., MCKENTY, P. W., MEYERHOFER, D. D., MYATT, J. F., SCHMITT, A. J., SETHIAN, J. D., SHORT, R. W., SKUPSKY, S., THEOBALD, W., KRUEER, W. L., TANAKA, K., BETTI, R., COLLINS, T. J. B., DELETTREZ, J. A., HU, S. X., MAROZAS, J. A., MAXIMOV, A. V., MICHEL, D. T., RADHA, P. B., REGAN, S. P., SANGSTER, T. C., SEKA, W., SOLODOV, A. A., SOURES, J. M., STOECKL, C. & ZUEGEL, J. D. 2015 Direct-drive inertial confinement fusion: A review. *Physics of Plasmas* **22** (11), 110501.
- CUI, YE, YANG, XIAO-HU, MA, YAN-YUN, ZHANG, GUO-BO, XU, BI-HAO, CHEN, ZE-HAO, LI, ZE, SHAO, FU-QIU & ZHANG, JIE 2024 The importance of righi-leduc heat flux on the ablative rayleigh-taylor instability during a laser irradiating targets. *High Power Laser Science and Engineering* p. 1–24.
- DAVIES, J. R., WEN, H., JI, JEONG-YOUNG & HELD, ERIC D. 2021 Transport coefficients for magnetic-field evolution in inviscid magnetohydrodynamics. *Physics of Plasmas* **28** (1), 012305.
- EPPERLEIN, E. M. & HAINES, M. G. 1986 Plasma transport coefficients in a magnetic field by direct numerical solution of the Fokker-Planck equation. *The Physics of Fluids* **29** (4), 1029–1041.
- FU, J. Y., ZHANG, H. S., CAI, H. B. & ZHU, S. P. 2023 Self-similar bubble-front evolutions of ablative Rayleigh-Taylor instability seeded by localized perturbations. *Physics of Plasmas* **30** (2), 022701.

- GAMEZO, VADIM N., KHOKHLOV, ALEXEI M., ORAN, ELAINE S., CHTCHELKANOVA, ALMADENA Y. & ROSENBERG, ROBERT O. 2003 Thermonuclear supernovae: Simulations of the deflagration stage and their implications. *Science* **299** (5603), 77–81.
- GAO, L., NILSON, P. M., IGUMENSCHEV, I. V., FIKSEL, G., YAN, R., DAVIES, J. R., MARTINEZ, D., SMALYUK, V., HAINES, M. G., BLACKMAN, E. G., FROULA, D. H., BETTI, R. & MEYERHOFER, D. D. 2013 Observation of self-similarity in the magnetic fields generated by the ablative nonlinear rayleigh-taylor instability. *Physical Review Letters* **110** (18), 1–5.
- GAO, L., NILSON, P. M., IGUMENSCHEV, I. V., HU, S. X., DAVIES, J. R., STOECKL, C., HAINES, M. G., FROULA, D. H., BETTI, R. & MEYERHOFER, D. D. 2012 Magnetic field generation by the Rayleigh-Taylor instability in laser-driven planar plastic targets. *Physical Review Letters* **109** (11), 1–5.
- GAO, L., NILSON, P. M., IGUMENSCHEV, I. V., HAINES, M. G., FROULA, D. H., BETTI, R. & MEYERHOFER, D. D. 2015 Precision mapping of laser-driven magnetic fields and their evolution in high-energy-density plasmas. *Physical Review Letters* **114** (21), 1–5.
- GARCÍA-RUBIO, F., BETTI, R., SANZ, J. & ALUIE, H. 2021 Magnetic-field generation and its effect on ablative Rayleigh-Taylor instability in diffusive ablation fronts. *Physics of Plasmas* **28** (1).
- GOMEZ, M. R., SLUTZ, S. A., SEFKOW, A. B., SINARS, D. B., HAHN, K. D., HANSEN, S. B., HARDING, E. C., KNAPP, P. F., SCHMIT, P. F., JENNINGS, C. A., AWE, T. J., GEISSEL, M., ROVANG, D. C., CHANDLER, G. A., COOPER, G. W., CUNEO, M. E., HARVEY-THOMPSON, A. J., HERRMANN, M. C., HESS, M. H., JOHNS, O., LAMPPA, D. C., MARTIN, M. R., MCBRIDE, R. D., PETERSON, K. J., PORTER, J. L., ROBERTSON, G. K., ROCHAU, G. A., RUIZ, C. L., SAVAGE, M. E., SMITH, I. C., STYGAR, W. A. & VESEY, R. A. 2014 Experimental demonstration of fusion-relevant conditions in magnetized liner inertial fusion. *Physical Review Letters* **113** (15), 1–5.
- GONCHAROV, V. N., BETTI, R., MCCRORY, R. L., SOROTOKIN, P. & VERDON, C. P. 1996a Self-consistent stability analysis of ablation fronts with large Froude numbers. *Physics of Plasmas* **3** (4), 1402–1414.
- GONCHAROV, V. N., BETTI, R., MCCRORY, R. L. & VERDON, C. P. 1996b Self-consistent stability analysis of ablation fronts with small Froude numbers. *Physics of Plasmas* **3** (12), 4665–4676.
- HAINES, M. G. 1985 Magnetic-Field Generation in Laser Fusion and Hot-Electron Transport. *Canadian journal of physics* **64** (8), 912–919.
- HARTEN, AMIRAM, LAX, PETER D. & LEER, BRAM VAN 1983 On upstream differencing and godunov-type schemes for hyperbolic conservation laws. *SIAM Review* **25** (1), 35–61.
- JI, JEONG-YOUNG & HELD, ERIC D. 2013 Closure and transport theory for high-collisionality electron-ion plasmas. *Physics of Plasmas* **20** (4), 042114, arXiv: https://pubs.aip.org/aip/pop/article-pdf/doi/10.1063/1.4801022/12468315/042114_1_online.pdf.
- VAN LEER, BRAM 1984 On the relation between the upwind-differencing schemes of godunov, engquist–osher and roe. *SIAM Journal on Scientific and Statistical Computing* **5** (1), 1–20.
- LI, C. K., SÉGUIN, F. H., FRENJE, J. A., RYGG, J. R., PETRASSO, R. D., TOWN, R. P.J., AMENDT, P. A., HATCHETT, S. P., LANDEN, O. L., MACKINNON, A. J., PATEL, P. K., TABAK, M., KNAUER, J. P., SANGSTER, T. C. & SMALYUK, V. A. 2007 Observation of the decay dynamics and instabilities of megagauss field structures in laser-produced plasmas. *Physical Review Letters* **99** (1).
- LI, C. K., SÉGUIN, F. H., FRENJE, J. A., MANUEL, M., CASEY, D., SINENIAN, N., PETRASSO, R. D., AMENDT, P. A., LANDEN, O. L., RYGG, J. R., TOWN, R. P.J., BETTI, R., DELETTREZ, J., KNAUER, J. P., MARSHALL, F., MEYERHOFER, D. D., SANGSTER, T. C., SHVARTS, D., SMALYUK, V. A., SOURES, J. M., BACK, C. A., KILKENNY, J. D. & NIKROO, A. 2009 Proton radiography of dynamic electric and magnetic fields in laser-produced high-energy-density plasmas. *Physics of Plasmas* **16** (5).
- LI, JUN, YAN, RUI, ZHAO, BIN, WU, JUNFENG, WANG, LIFENG & ZOU, SHIYANG 2024 Effect of hot-electron preheating on the multimode bubble-front growth of the ablative Rayleigh–Taylor instability. *Physics of Plasmas* **31** (1), 012703.
- LI, JUN, YAN, RUI, ZHAO, BIN, ZHENG, JIAN, ZHANG, HUASEN & LU, XIYUN 2022 Mitigation of the ablative Rayleigh–Taylor instability by nonlocal electron heat transport. *Matter and Radiation at Extremes* **7** (5), 055902.
- LI, JUN, YAN, RUI, ZHAO, BIN, ZHENG, JIAN, ZHANG, HUASEN & LU, XIYUN 2023 Role of hot electrons in mitigating ablative Rayleigh–Taylor instability. *Physics of Plasmas* **30** (2), 022706.

- LINDL, JOHN 1995 Development of the indirect-drive approach to inertial confinement fusion and the target physics basis for ignition and gain. *Physics of Plasmas* **2** (11), 3933–4024.
- LINDL, J. D. 1998 *Inertial Confinement Fusion*. Springer New York.
- LINDL, JOHN D., AMENDT, PETER, BERGER, RICHARD L., GLENDINNING, S. GAIL, GLENZER, SIEGFRIED H., HAAN, STEVEN W., KAUFFMAN, ROBERT L., LANDEN, OTTO L. & SUTER, LAURENCE J. 2004 The physics basis for ignition using indirect-drive targets on the National Ignition Facility. *Physics of Plasmas* **11** (2), 339–491.
- LIU, YANG, ZHANG, DE-HUA, XIN, JING-FEI, PU, YUDONG, LI, JUN, TAO, TAO, SUN, DEJUN, YAN, RUI & ZHENG, JIAN 2023 Growth of ablative Rayleigh-Taylor instability induced by time-varying heat-flux perturbation. *Matter and Radiation at Extremes* **9** (1), 016603.
- MANUEL, M. J.E., FLAIG, M., PLEWA, T., LI, C. K., SÉGUIN, F. H., FRENJE, J. A., CASEY, D. T., PETRASSO, R. D., HU, S. X., BETTI, R., HAGER, J., MEYERHOFER, D. D. & SMALYUK, V. 2015 Collisional effects on Rayleigh-Taylor-induced magnetic fields. *Physics of Plasmas* **22** (5).
- MANUEL, M. J.E., LI, C. K., SÉGUIN, F. H., FRENJE, J., CASEY, D. T., PETRASSO, R. D., HU, S. X., BETTI, R., HAGER, J. D., MEYERHOFER, D. D. & SMALYUK, V. A. 2012 First measurements of Rayleigh-Taylor-induced magnetic fields in laser-produced plasmas. *Physical Review Letters* **108** (25), 1–5.
- MATSUO, KAZUKI, SANO, TAKAYOSHI, NAGATOMO, HIDEO, SOMEKAWA, TOSHIHIRO, LAW, KING FAI FARLEY, MORITA, HIROKI, ARIKAWA, YASUNOBU & FUJIOKA, SHINSUKE 2021 Enhancement of ablative Rayleigh-Taylor instability growth by thermal conduction suppression in a magnetic field. *Physical Review Letters* **127** (16), 165001.
- MCKENTY, P. W., GONCHAROV, V. N., TOWN, R. P. J., SKUPSKY, S., BETTI, R. & MCCRORY, R. L. 2001 Analysis of a direct-drive ignition capsule designed for the National Ignition Facility. *Physics of Plasmas* **8** (5), 2315.
- MIMA, K., TAJIMA, T. & LEBOEUF, J. N. 1978 Magnetic field generation by the Rayleigh-Taylor instability. *Physical Review Letters* **41** (25), 1715–1719.
- MOODY, J. D., POLLOCK, B. B., SIO, H., STROZZI, D. J., HO, D. D.M., WALSH, C. A., KEMP, G. E., LAHMANN, B., KUCHEYEV, S. O., KOZIOZIEMSKI, B., CARROLL, E. G., KROLL, J., YANAGISAWA, D. K., ANGUS, J., BACHMANN, B., BHANDARKAR, S. D., BUDE, J. D., DIVOL, L., FERGUSON, B., FRY, J., HAGLER, L., HARTOUNI, E., HERRMANN, M. C., HSING, W., HOLUNGA, D. M., IZUMI, N., JAVEDANI, J., JOHNSON, A., KHAN, S., KALANTAR, D., KOHUT, T., LOGAN, B. G., MASTERS, N., NIKROO, A., ORSI, N., PISTON, K., PROVENCHER, C., ROWE, A., SATER, J., SKULINA, K., STYGAR, W. A., TANG, V., WINTERS, S. E., ZIMMERMAN, G., ADRIAN, P., CHITTENDEN, J. P., APPELBE, B., BOXALL, A., CRILLY, A., O’NEILL, S., DAVIES, J., PEEBLES, J. & FUJIOKA, S. 2022 Increased Ion Temperature and Neutron Yield Observed in Magnetized Indirectly Driven D2 -Filled Capsule Implosions on the National Ignition Facility. *Physical Review Letters* **129** (19), 195002.
- NISHIGUCHI, A., YABE, T. & HAINES, M. G. 1985 Nernst effect in laser-produced plasmas. *Physics of Fluids* **28** (12), 3683–3690.
- NISHIGUCHI, A., YABE, T., HAINES, M. G., PSIMOPOULOS, M. & TAKEWAKI, H. 1984 Convective amplification of magnetic fields in laser-produced plasmas by the Nernst effect. *Physical Review Letters* **53** (3), 262–265.
- PERKINS, L. J., HO, D. D.M., LOGAN, B. G., ZIMMERMAN, G. B., RHODES, M. A., STROZZI, D. J., BLACKFIELD, D. T. & HAWKINS, S. A. 2017 The potential of imposed magnetic fields for enhancing ignition probability and fusion energy yield in indirect-drive inertial confinement fusion. *Physics of Plasmas* **24** (6).
- RAVEN, A., WILLI, O. & RUMSBY, P. T. 1978 Megagauss magnetic field profiles in laser-produced plasmas. *Physical Review Letters* **41** (8), 554–557.
- RAYLEIGH, LORD 1900 *Scientific Papers II* (Cambridge University Press, Cambridge, England) p. 200.
- SADLER, JAMES D., WALSH, CHRISTOPHER A. & LI, HUI 2021 Symmetric set of transport coefficients for collisional magnetized plasma. *Phys. Rev. Lett.* **126**, 075001.
- SANZ, J. 1994 Self-consistent Analytical Model of the Rayleigh-Taylor Instability in Inertial Confinement Fusion. *Physical Review Letters* **73** (2700–2703), 1919–1922.
- SIO, H., MOODY, J. D., POLLOCK, B. B., STROZZI, D. J., HO, D. D.M., WALSH, C. A., KEMP, G. E., LAHMANN, B., KUCHEYEV, S. O., KOZIOZIEMSKI, B., CARROLL, E. G., KROLL, J., YANAGISAWA, D. K., ANGUS, J., BACHMANN, B., BAKER, A. A., BAYU AJI, L. B., BHANDARKAR, S. D., BUDE, J. D., DIVOL, L., ENGWALL, A. M., FERGUSON, B., FRY, J., HAGLER, L., HARTOUNI, E., HERRMANN, M. C., HSING, W., HOLUNGA, D. M., JAVEDANI, J.,

- JOHNSON, A., KHAN, S., KALANTAR, D., KOHUT, T., LOGAN, B. G., MASTERS, N., NIKROO, A., IZUMI, N., ORSI, N., PISTON, K., PROVENCHER, C., ROWE, A., SATER, J., SHIN, S. J., SKULINA, K., STYGAR, W. A., TANG, V., WINTERS, S. E., ZIMMERMAN, G., CHITTENDEN, J. P., APPELBE, B., BOXALL, A., CRILLY, A., O'NEILL, S., BARNAK, D., DAVIES, J., PEEBLES, J., BAE, J. H., CLARK, K., HAVRE, M., MAULDIN, M., RATLEDGE, M., VONHOF, S., ADRIAN, P., REICHEL, B., FUJIOKA, S. & FRAENKEL, M. 2023 Performance scaling with an applied magnetic field in indirect-drive inertial confinement fusion implosions. *Physics of Plasmas* **30** (7).
- SLUTZ, STEPHEN A. & VESEY, ROGER A. 2012 High-gain magnetized inertial fusion. *Physical Review Letters* **108** (2), 1–5.
- SPITZER, LYMAN & HÄRM, RICHARD 1953 Transport phenomena in a completely ionized gas. *Phys. Rev.* **89**, 977–981.
- SRINIVASAN, BHUVANA, DIMONTE, GUY & TANG, XIAN ZHU 2012 Magnetic field generation in Rayleigh-Taylor unstable inertial confinement fusion plasmas. *Physical Review Letters* **108** (16), 1–5.
- SRINIVASAN, BHUVANA & TANG, XIAN ZHU 2012 Mechanism for magnetic field generation and growth in Rayleigh-Taylor unstable inertial confinement fusion plasmas. *Physics of Plasmas* **19** (8).
- SRINIVASAN, BHUVANA & TANG, XIAN ZHU 2013 The mitigating effect of magnetic fields on Rayleigh-Taylor unstable inertial confinement fusion plasmas. *Physics of Plasmas* **20** (5).
- STAMPER, J. A. 1991 Review on spontaneous magnetic fields in laser-produced plasmas: Phenomena and measurements. *Laser and Particle Beams* **9** (4), 841–862.
- STAMPER, J. A., MCLEAN, E. A. & RIPIN, B. H. 1978 Studies of spontaneous magnetic fields in laser-produced plasmas by Faraday rotation. *Physical Review Letters* **40** (18), 1177–1181.
- STAMPER, J. A., PAPADOPOULOS, K., SUDAN, R. N., DEAN, S. O., MCLEAN, E. A. & DAWSON, J. M. 1971 Spontaneous Magnetic Fields in Laser-Produced Plasmas. *Physical Review Letters* **26** (17), 1012–1015.
- STAMPER, J. A. & RIPIN, B. H. 1975 Faraday-rotation measurements of megagauss magnetic fields in laser-produced plasmas. *Physical Review Letters* **34** (3), 138–141.
- STRANG, GILBERT 1968 On the construction and comparison of difference schemes. *SIAM journal on numerical analysis* **5** (3), 506–517.
- TAKABE, H., MIMA, K., MONTIERTH, L. & MORSE, R. L. 1985 Self-consistent growth rate of the Rayleigh-Taylor instability in an ablatively accelerating plasma. *Physics of Fluids* **28** (12), 3676–3682.
- TAYLOR, G. 1950 The instability of liquid surfaces when accelerated in a direction perpendicular to their planes. i. *Proceedings of the Royal Society of London* **201** (1065), 192–196.
- WAGNER, U., TATARAKIS, M., GOPAL, A., BEG, F. N., CLARK, E. L., DANGOR, A. E., EVANS, R. G., HAINES, M. G., MANGLES, S. P.D., NORREYS, P. A., WEI, M. S., ZEPF, M. & KRUSHELNICK, K. 2004 Laboratory measurements of [Formula presented] magnetic fields generated during high-intensity laser interactions with dense plasmas. *Physical Review E - Statistical Physics, Plasmas, Fluids, and Related Interdisciplinary Topics* **70** (2), 5.
- WALSH, C. A. 2022 Magnetized ablative Rayleigh-Taylor instability in three dimensions. *Physical Review E* **105** (2), 1–9.
- WALSH, C. A., CHITTENDEN, J. P., MCGLINCHEY, K., NIASSE, N. P. L. & APPELBE, B. D. 2017 Self-generated magnetic fields in the stagnation phase of indirect-drive implosions on the national ignition facility. *Phys. Rev. Lett.* **118**, 155001.
- WURDEN, G. A., HSU, S. C., INTRATOR, T. P., GRABOWSKI, T. C., DEGNAN, J. H., DOMONKOS, M., TURCHI, P. J., CAMPBELL, E. M., SINARS, D. B., HERRMANN, M. C., BETTI, R., BAUER, B. S., LINDEMUTH, I. R., SIEMON, R. E., MILLER, R. L., LABERGE, M. & DELAGE, M. 2016 Magneto-Inertial Fusion. *Journal of Fusion Energy* **35** (1), 69–77.
- XIN, J., LIU, Y., JIANG, X., YAN, R., LI, J., WAN, Z.-H., SUN, D.-J. & ZHENG, J. 2023 Effects of ablation velocity on ablative Rayleigh-Taylor instability. *Physics of Plasmas* **30** (11), 112702.
- XIN, J., YAN, R., WAN, Z. H., SUN, D. J., ZHENG, J., ZHANG, H., ALUIE, H. & BETTI, R. 2019 Two mode coupling of the ablative Rayleigh-Taylor instabilities. *Physics of Plasmas* **26** (3).
- YAN, R., BETTI, R., SANZ, J., ALUIE, H., LIU, B. & FRANK, A. 2016 Three-dimensional single-mode nonlinear ablative Rayleigh-Taylor instability. *Physics of Plasmas* **23** (2).
- ZHANG, D., LI, J., XIN, J., YAN, R., WAN, Z., ZHANG, H. & ZHENG, J. 2022 Self-generated magnetic field in ablative Rayleigh-Taylor instability. *Physics of Plasmas* **29** (7), 072702.
- ZHANG, HUASEN, BETTI, R., YAN, RUI & ALUIE, H. 2020 Nonlinear bubble competition of the

- multimode ablative Rayleigh–Taylor instability and applications to inertial confinement fusion. *Physics of Plasmas* **27** (12), 122701.
- ZHANG, H., BETTI, R., YAN, R., ZHAO, D., SHVARTS, D. & ALUIE, H. 2018 Self-Similar Multimode Bubble-Front Evolution of the Ablative Rayleigh-Taylor Instability in Two and Three Dimensions. *Physical Review Letters* **121** (18), 185002.
- ZYLSTRA, AB, HURRICANE, OA, CALLAHAN, DA, KRITCHER, AL, RALPH, JE, ROBNEY, HF, ROSS, JS, YOUNG, CV, BAKER, KL, CASEY, DT & OTHERS 2022 Burning plasma achieved in inertial fusion. *Nature* **601** (7894), 542–548.